Chapter 5

The RFQ Calibration

The L3 detector was built with a specific purpose: to look for manifestations of new physics using precision measurements of photons and leptons [128]. The L3 BGO calorimeter stood prominently as the most accurate photon detector at LEP (see Section 4.2.3 p. 80). For example, L3 was the only experiment to observe the χ_{c1} meson at LEP via the reaction $\mathrm{Z} \to \chi_{c1} + \mathrm{X}$, $\chi_{c1} \to J/\Psi\, \gamma$, $J/\Psi \to \mathrm{e}^+\mathrm{e}^-, \mu^+\mu^-$ [129]. The resulting measurement of the branching fraction $\mathrm{Br}(\mathrm{Z} \to \chi_{c1} + \mathrm{X})$ is still the most accurate available.

In Section 4.2.3 I summarized the construction principle, the geometry, and the readout chain of the BGO calorimeter. In this chapter, I describe its calibration and monitoring as well as its particle reconstruction algorithm. In particular, the RFQ calibration technique, which provided the most precise calibration at LEP, is discussed in detail.

5.1 Particle Reconstruction in the BGO

The BGO calorimeter was designed to measure the energy and direction of the showers produced by particles traversing the BGO crystals. The shower shape parameters can be used to classify such particles as either particles producing electromagnetic showers (electrons, positrons or photons), particles producing minimum ionizing signals (mostly muons), or particles with mainly hadronic interactions.

The design of the BGO was optimized for photons and electrons which could be precisely reconstructed as they generated compact electromagnetic showers with little shape variation. Such showers were almost fully contained in the BGO material.

The rear-end leakage was determined to be below 2% even for 45 GeV electrons (see Section 6.3.6). Hadrons lost their energy in the BGO through ionization and nuclear interactions, developing showers with larger fluctuations and significant leakage (the BGO material represented only one nuclear interaction length). Relativistic muons did not interact strongly with the BGO material and produced small signals,[1] which were a slowly varying function of the muon energy [6].

The first step of the particle reconstruction algorithm was to convert a raw ADC signal of each BGO crystal into a corresponding energy value. The transformation for a crystal k is given by

$$E_k = C_k \cdot (A_k - P_k), \tag{5.1}$$

where

- E_k is the energy deposited in this crystal
- C_k is the calibration constant for this crystal
- A_k is the ADC signal
- P_k is the ADC pedestal.

The pedestals for all channels were updated on a daily basis and were obtained using a special type of calibration runs (*BASE* runs), which were performed between LEP fills. In contrast, the calibration constants were usually determined twice each year — before and after the LEP annual run.

The second stage of the particle reconstruction algorithm involved building a map of all individual energy depositions to localize showers in the BGO. Crystals with significant energy depositions were grouped into clusters, defined as a set of adjacent crystals with an energy of more than 10 MeV per crystal. Then, in each cluster local maxima (*bump crystals*) were identified and the remaining crystals were attached to the bump crystals to form *BGO bumps*. Bump crystals were required to have energy greater than 40 MeV and be more energetic than the 8 neighboring crystals in the

---

[1] Multi-GeV muons traversing the full length of the crystal deposited on average between 200 and 250 MeV [108].

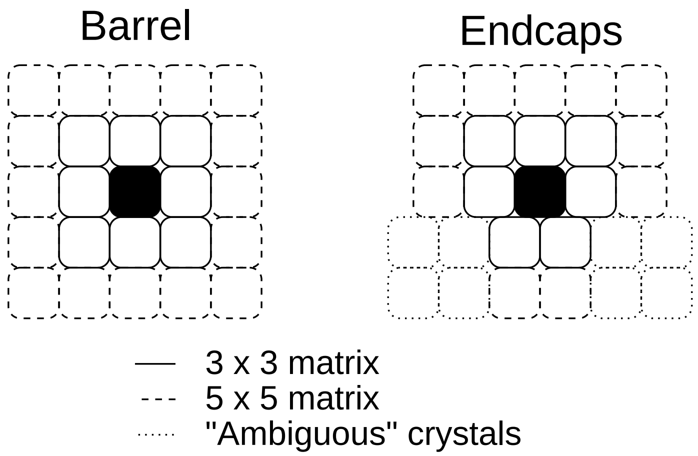

Figure 5.1: Crystals forming 3×3 and 5×5 matrices in the barrel and in the endcaps.

3×3 matrix. The non-bump crystals were assigned to the nearest bump crystal in the same cluster. If a crystal was equidistant to two bump crystals, it was assigned to the most energetic one.

Each BGO bump was assumed to correspond to a particle traversing the calorimeter, and the energy of such particle was calculated using the following quantities:

$$S_1 \equiv E_1 \;, \qquad S_9 \equiv \sum_{3\times3} E_i \;, \qquad S_{25} \equiv \sum_{5\times5} E_i \;,$$

where E_1 is the energy of the bump crystal and the sums range over crystals in the 3×3 and 5×5 matrices centered on the bump crystal. The layout of these matrices is shown in Figure 5.1. In the endcap regions where crystals were not aligned in ϕ across different θ-rings, some care had to be taken in creating the 3×3 and 5×5 matrices. A special algorithm was implemented to extend the $n \times n$ matrix in the following way. For each new θ-ring the middle crystal was chosen to be the one with ϕ closest the ϕ-position of the central crystal. When two crystals had the same $\Delta\phi$, the one with the highest energy was chosen as the middle one of this θ-ring.

During the R&D tests, prior to and during the construction of the BGO calorimeter, extensive studies of the electromagnetic shower development and containment in the BGO crystals were performed using both beam tests and MC simulations [130].

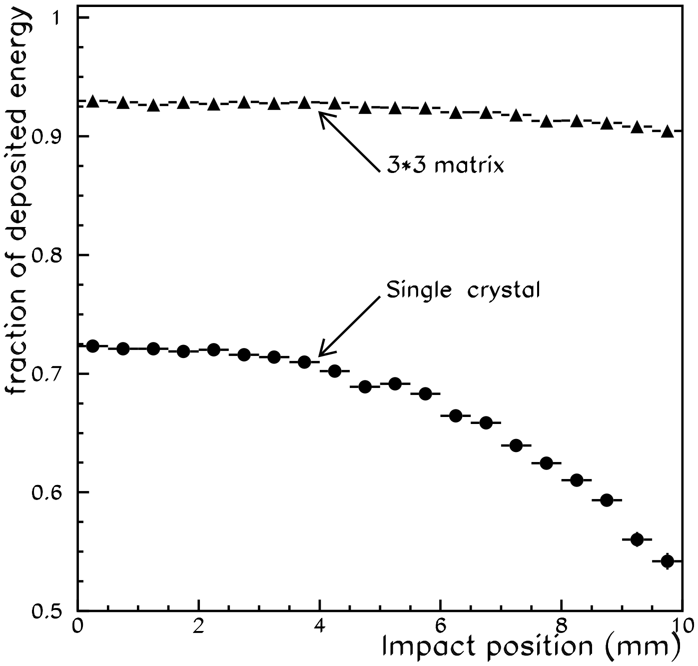

Figure 5.2: The fraction of the shower energy deposited in the central crystal and in the 3×3 crystal matrix as a function of the distance from the impact point to the crystal center [131].

On average, electromagnetic showers from electrons incident on the crystal axis would deposit about 75% of energy in the central crystal and about 94% and 97% of energy in the 3×3 and 5×5 matrices, respectively. A first approximation of the shower energy can therefore be obtained using S_9 or S_{25} energy sums scaled by an appropriate constant factor.

The lateral energy loss due to the finite crystal size and the gaps between the crystals depends on the impact point position. Therefore the shower profile also depends on the position of the impact with respect to the crystal center. Figure 5.2 shows this dependence for the fractional energies S_1/E_{shower} and S_9/E_{shower} as determined during the beam tests[2] [131]. It was noticed that the lateral energy leakage was correlated with the ratio S_1/S_9, and a *corrected sum-of-nine* energy was defined as

$$S_9^c = \frac{S_9}{c_1(\theta) \cdot S_1/S_9 + c_2(\theta)}, \tag{5.2}$$

---

[2] The test beam studies are described in the next section.

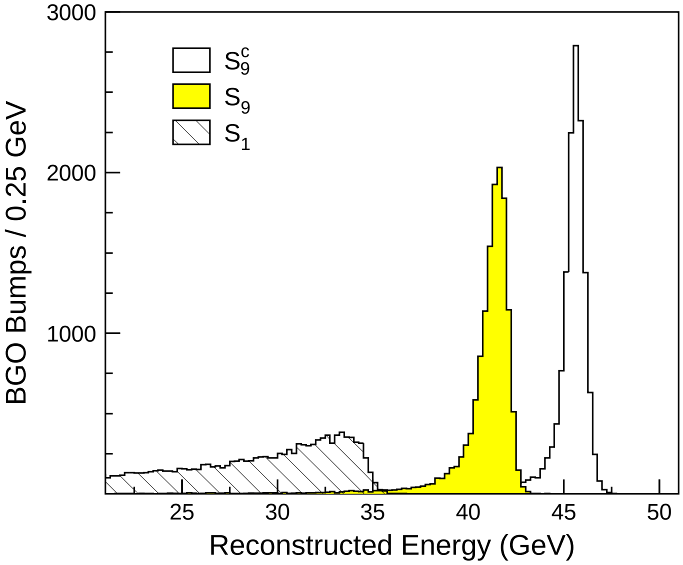

Figure 5.3: Distributions of the energy quantities S_1, S_9 and S_9^c reconstructed for the 45.6 GeV Bhabha electrons.

where the parameters $c_1(\theta)$ and $c_2(\theta)$ are θ-dependent coefficients. They were chosen to satisfy $\langle S_9^c\rangle \simeq E_{incident}$, where $E_{incident}$ was the energy of the incident beam of electrons. Numerically, c_1 is 0.1231 and c_2 is 0.8222 for the barrel, while in the endcaps $c_1 = 0.065 + F_1(\theta)$ and $c_2 = 0.865 + F_2(\theta)$. $F_1(\theta)$ and $F_2(\theta)$ are θ-dependent functions of the order of a few percent. Figure 5.3 shows the distributions of S_1, S_9, and S_9^c for 45.6 GeV electrons selected using the Bhabha scattering process, $e^+e^- \rightarrow e^+e^-$. One can see that S_9^c provides a clear improvement in the energy resolution.

In a similar fashion, a *corrected sum-of-25* (S_{25}^c) can be constructed using quantities S_1 and S_{25}. Because the electromagnetic showers are almost fully contained in the 3×3 crystal matrix, the S_{25}^c variable gives the same energy resolution as S_9^c for showers with $E_{shower} > 50$ GeV. For showers with smaller energy depositions, the use of S_9^c is preferred since this quantity is less affected by the BGO electronic noise and the (possible) presence of dead channels in the crystal matrices. However, the S_{25}^c quantity proved to be very useful in distinguishing between electromagnetic showers and showers originating from hadrons and cosmic rays (as discussed in the next chapter).

To reconstruct the impact point of the incident particles, the following procedure is used. First, the center-of-gravity of the bump is calculated using the the energy depositions in the 3×3 crystal matrix and the actual positions of the crystal front faces θ_i and ϕ_i:

$$\Theta_{cog} = \frac{\sum_{i=1}^{9} \theta_i E_i}{S_9} \qquad \Phi_{cog} = \frac{\sum_{i=1}^{9} \phi_i E_i}{S_9} \ .$$

The center-of-gravity is displaced from the true impact point due to the granularity of the calorimeter. Because the bump crystal has a very large weight in this sum, the center-of-gravity is always shifted to the center of the bump crystal. This effect can be taken into account using a correction function determined in beam tests, where the beam position could be measured with proportional chambers placed in front of the crystal matrix. The correction function is given by

$$x_{impact} = \alpha \tan \beta x_{cog} + \gamma x_{cog} \qquad y_{impact} = \alpha \tan \beta y_{cog} + \gamma y_{cog} \ ,$$

where x and y are given in the local Cartesian coordinate system with the center of bump crystal at the origin, and $\alpha = 6.0288$ mm, $\beta = 0.53$ mm^{-1}, and $\gamma = 0.215$. This procedure was proven to work very well for electromagnetic bumps in the energy range studied in this thesis [132].

5.2 Test Beam Studies

In 1987-88, prior to their installation in L3, both BGO half-barrels and a part of the endcaps were extensively studied [131] in the X3 beam line of the CERN super proton synchrotron (SPS).[3] Electron beams at four energies, 2, 10, 20, and 50 GeV, were used. One half-barrel was also tested using a 180 MeV electron beam extracted from the LEP injector Linac. The half-barrels were installed on a rotating table so that each crystal could be calibrated individually. A position accuracy of less than 1 mm was achieved, and the angle between the beam and longitudinal axis of the crystal was determined to be less than 5 mrad.

---

[3] The SPS was also a part of the LEP injector chain, which was described in detail in Section 4.1.1.

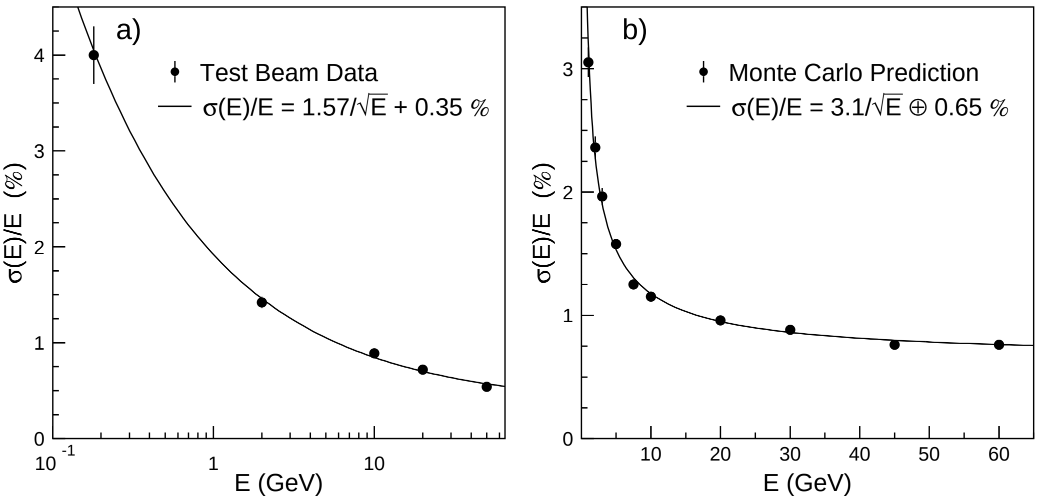

Figure 5.4: BGO energy resolution curves from a) test beam precalibration and b) Monte Carlo simulations.

The test beam studies were conducted to achieve the following objectives: to study the shower profile characteristics,[4] to calibrate each BGO crystal, and to measure the energy and angular resolutions of the calorimeter. About 800 events per crystal were collected, and the calibration constants were determined with an accuracy of 0.5%. Since the crystals were calibrated in the final configuration and with the final readout electronics, the obtained calibration constants were actually used at the beginning of the LEP physics program.

For each value of the beam energy, the overall energy resolution in the barrel was estimated by fitting the combined shower energy distributions of all crystals. After subtracting contributions from the calibration and beam energy errors, the BGO energy resolution was parametrized as

$$\frac{\sigma_E}{E}(\text{Test beam}) = \frac{1.6 \pm 0.1\ \%}{\sqrt{E}} + 0.35 \pm 0.05\ \%\ (E \text{ in GeV}). \tag{5.3}$$

The test beam measurements and the fitted resolution curve are shown in Figure 5.4a.

The energy resolution can also be studied using large samples of electrons gener-

---

[4] The results of the shower development studies were already used in the previous section.

ated using the *ideal* L3 Monte Carlo program. This program simulates the electromagnetic shower development in the BGO under the assumption of perfectly known calibration constants. The obtained energy resolution as a function of shower energy, shown in Figure 5.4b, is best fitted with[5]

$$\frac{\sigma_E}{E}(\mathrm{MC}) = \frac{3.1 \pm 0.1\ \%}{\sqrt{E}} \oplus 0.65 \pm 0.03\ \%\ (E \text{ in GeV})\,, \tag{5.4}$$

where the first term is expected to be mainly due to photostatistics fluctuations and the second term comes from shower containment limitations and calorimeter non-uniformities [133].

Naively, one would expect this resolution function to be in agreement with the one obtained with the test beams. However, one can see that this is not the case. For example, for 45 GeV showers the BGO energy resolution obtained using Monte Carlo simulation is expected to be about 0.9%, which is much worse than the 0.5% resolution obtained with the test beam. Moreover, the *in situ* energy resolution at the beginning of the LEP1 physics program was measured to be about 1.4% [134]. The reason for this discrepancy is the difference between the bump selection criteria used in the test beam precalibration and *in situ* at LEP. Only bumps with an impact point within 5 mm from the crystal center, $R_{impact} < 5$ mm, were selected in test beams studies. This very severe cut was not applied in the analysis of LEP data, as it would reject about 80% of electromagnetic showers.

In order to verify that this is indeed the cause of the discrepancy, I used a sample of about 6,600 Bhabha electrons with an energy of about 103 GeVwhich I selected in high energy data collected by L3 in the year 2000.[6] Figure 5.2 shows that the quantity S_1 decreases faster with increasing R_{impact} as compared to the quantity S_9. Thus, the ratio S_1/S_9 can be used to estimate R_{impact} and, as shown in Reference [135], the cut on the impact position applied in the test beam studies is equivalent to $S_1/S_9 > 0.8$ The distribution of S_1/S_9 for data and Monte Carlo is shown in Figure 5.5a, and the

---

[5] The symbol "$\oplus$" denotes the quadratic sum.

[6] The selection of Bhabha events is described in detail in Section 5.6.2.

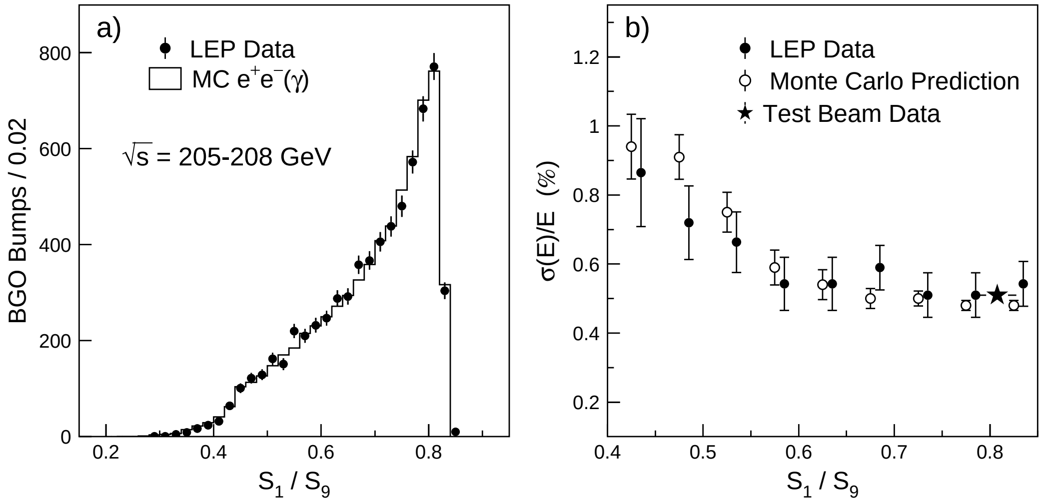

Figure 5.5: a) Distribution of S_1/S_9 for 103 GeV electrons. b) BGO energy resolution as a function of S_1/S_9 derived from LEP data, Monte Carlo simulation, and test beam studies. For clarity, the data points are slightly displaced horizontally.

obtained BGO energy resolution[7] as a function of S_1/S_9 is plotted in Figure 5.5b. A good agreement between measurements with LEP data and Monte Carlo predictions is observed. It is also important to note that for bumps with $S_1/S_9 > 0.8$, the resolution given by Monte Carlo simulation agrees well with the resolution measured in the test beam precalibration. Therefore, it can be concluded that the energy dependence of the BGO intrinsic resolution is better described by Equation 5.4. The validity of this equation is further confirmed in Section 5.6.2.

5.3 Monitoring of the BGO Calorimeter

In this section, I describe several techniques and systems used to monitor the BGO calorimeter at LEP. These include the temperature control and monitoring systems, the Xenon calibration system, and the detection of dead BGO channels. I also discuss problems with the BGO calibration at the beginning of the LEP2 phase and the need for a more precise calibration.

---

[7] The resolution measurement procedure is explained in Section C.1.

5.3.1 Temperature Control and Monitoring

The BGO light yield is temperature dependent; it decreases with increasing temperature with a coefficient of $-1.55\%/^\circ\mathrm{C}$. Therefore, in order to achieve the designed energy resolution it was necessary to carefully control and monitor the BGO temperature. The temperature control was provided by active thermal shields consisting of brass screens to which copper pipes carrying a silicone-based coolant were soldered. These shields were used to dissipate the heat generated by preamplifiers and first-level boards (2 W per channel) and to prevent heat transfer from the BGO to the neighboring subdetectors.

Year	Barrel RB24		Barrel RB26		Endcap RB24		Endcap RB26	
	T_{front}	T_{back}	T_{front}	T_{back}	T_{front}	T_{back}	T_{front}	T_{back}
1998	17.11	16.94	16.97	16.94	17.49	17.50	16.98	17.49
1999	17.02	16.88	16.99	17.01	17.39	17.39	16.89	17.49
2000	17.01	16.89	16.90	16.91	17.28	17.31	16.92	17.39

Table 5.1: Mean temperatures (in °C) of the front and back surfaces of the four BGO subdetectors. The results are given as the annual averages for each year during the period 1998-2000.

The temperature monitoring was performed using 1792 2AD590 sensors (1280 in the barrel and 2×256 in the endcaps) with a reading accuracy of 0.1°C. They were positioned on the front and rear faces of one in every 12 BGO crystals. The temperature sensor data was digitized and read out in the same as way as the crystal light output data. The annual average front and back temperatures of the four BGO subdetectors are given in Table 5.1 for the period 1998-2000. This table shows that the average BGO temperature was about 17°C and its variations from year to year were below 0.1°C. It also shows that the average temperature gradient between the front and back surfaces was maintained to be at most a few tenths of a degree.

The BGO temperature was usually measured once a day, and the temperature map for the front and rear faces of the entire calorimeter was computed by fitting the sensor data to the Laplace's equation for heat transfer, $\nabla^2 T(\vec{r}) = 0$. The distributions of the front BGO temperature from a typical fit in 2000 are shown in Figures 5.6a

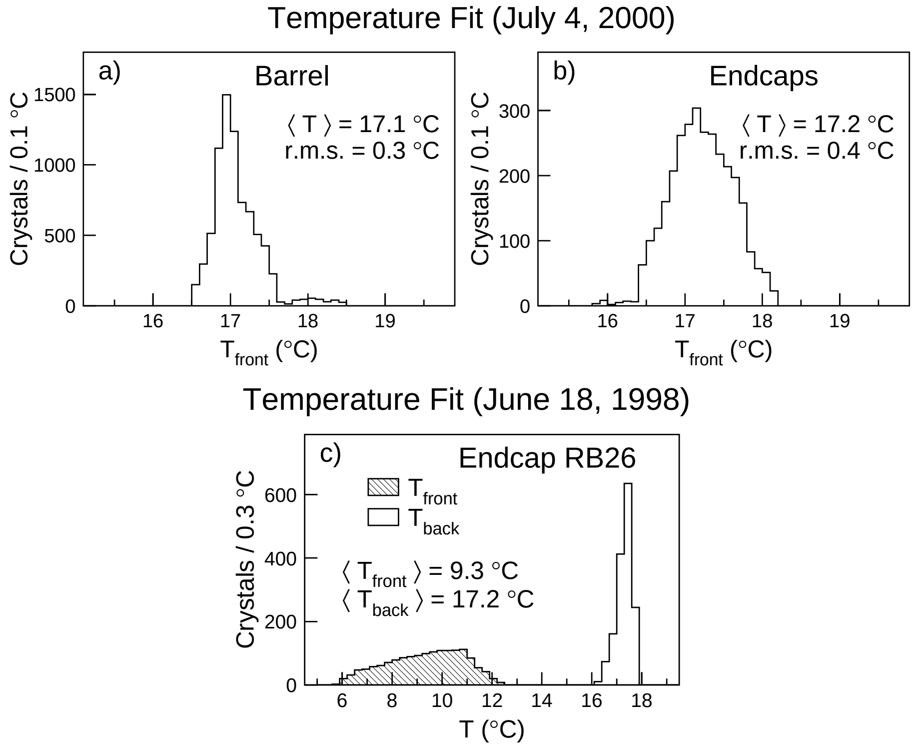

Figure 5.6: Distribution of the front BGO temperature, (a) in the barrel and (b) in the endcaps, from a typical temperature fit in 2000. (c) Distributions of the front and back BGO temperatures of the RB26 endcap from a typical "bad" temperature fit in 1998.

and 5.6b for the barrel and the endcaps, respectively. The energy reconstructed in a BGO crystal, as given by Equation 5.1, should then be multiplied by a temperature correction factor which is given by

$$C_T = 1 + 0.0155 \cdot (T_{max} - T_0), \quad T_{max} = T_{front} + \eta(E) \cdot \ (T_{back} - T_{front}), \tag{5.5}$$

where T_0 is the reference temperature (chosen to be 18°C), T_{max} is the temperature at the location of shower maximum, T_{front} and T_{back} are the temperatures of the front and back crystal surfaces, and $\eta(E)$ denotes the longitudinal position of the shower maximum relative to the crystal length. The relative shower depth is energy dependent, and the reference values of $\eta(E)$ were determined to be $\eta(2\text{ GeV}) = 0.21$, $\eta(10\text{ GeV}) = 0.27$, and $\eta(50\text{ GeV}) = 0.33$ [131].

The fit uncertainty on the surface temperatures of a given BGO crystal was estimated to be 0.3°C [136]. The relative error on the temperature correction factor for the shower energy measurement can be then calculated from Equations 5.2 and 5.5 and is equal to about 0.5%. The actual uncertainty contributing to the BGO energy resolution may be slightly higher due to the aging of the temperature sensors.[8] It was estimated that during the LEP2 phase (1996-2000), 5-10% of the temperature sensors were either dead or provided unreliable data.

The number of such sensors was particularly high on the front side of the RB26 endcap,[9] where it led to the problem of so-called "bad" temperature fits. Figure 5.6c shows distributions of the front and back temperatures from a "bad" fit in 1998. As can be seen from this figure, the average back temperature is close to the expected value of about 17°C, whereas the front temperatures are given to be in the range of 6-12°C. This significant difference between the front and back temperatures was caused by several front sensors which produced unphysically low temperature readings.[10] In total, "bad" temperature fits affected about 6% of L3 data in 1997-1998, which gave rise to a clear secondary peak at $E_{shower}/E_{beam} \approx 0.85$ in the energy distribution for Bhabha electrons reconstructed in the RB26 endcap. I first noticed this effect in 1998 when I was selecting Bhabha events to test the RFQ calibration of the BGO calorimeter. I then carried out a study of the reliability of the BGO temperature monitoring and corrected the "bad" fits in the L3 database. During 1998-2000 I was responsible for monitoring the performance of the BGO temperature control system.

5.3.2 Dead Crystals

During the twelve years of BGO calorimeter operation at LEP, a certain number of readout channels started to malfunction and did not provide reliable readings. The appearance of such channels, which were usually referred to as *dead crystals*, was caused by malfunctioning photodiodes or preamplifiers and not by problems with the BGO crystals themselves. Since the BGO calorimeter was not accessible at LEP, the

---

[8] The study of the temperature fit uncertainty was performed in 1994 [136].

[9] The two halves of the L3 detector are traditionally referred to as RB26 and RB24.

[10] For instance, several "bad" fits produced sub-zero temperatures.

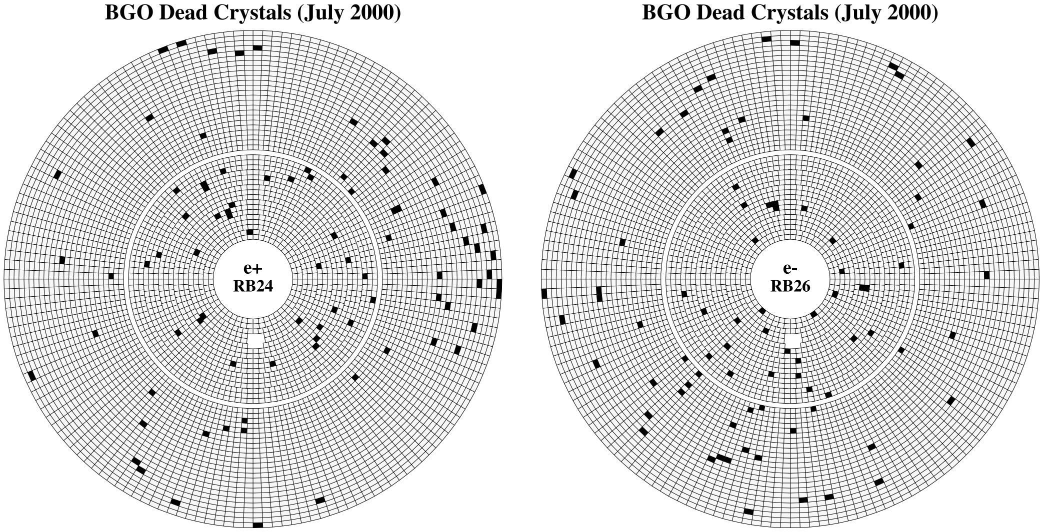

Figure 5.7: Distributions of the dead channels for the two sides of the BGO calorimeter. The dead crystals are shown as black squares and the inner and outer rings represent the endcaps and half-barrels, respectively.

readout electronics could not be repaired and the dead crystals had to be dropped from the standard BGO reconstruction.

The number of dead crystals was almost constant during the LEP2 phase and amounted to about 1.5% of the total BGO channels (about 100 channels in the barrel and 60 channels in the endcaps) [137]. The majority of the dead crystals were identified online with Xenon flashlamps, as described in the next section. The remaining dead crystals were detected offline using large samples of events with high multiplicity hadronic jets. Such events provided azimuthally-independent irradiation of the BGO calorimeter and the malfunctioning channels could be identified as deviations in the crystal occupancy distributions of the individual BGO θ-rings [135]. An additional class of dead channels was found during the first RFQ calibration in 1997. While investigating the problem of hard resolution tails, I found that the long tail, above $E_{shower}/E_{beam} = 1.1$, of the Bhabha energy distribution was caused to a large extent by about 20 crystals with mismeasured pedestals,[11] which were then also discarded from the BGO reconstruction.

---

[11] This problem was caused by a bug in the pedestal measurement algorithm, which had been overlooked at LEP1.

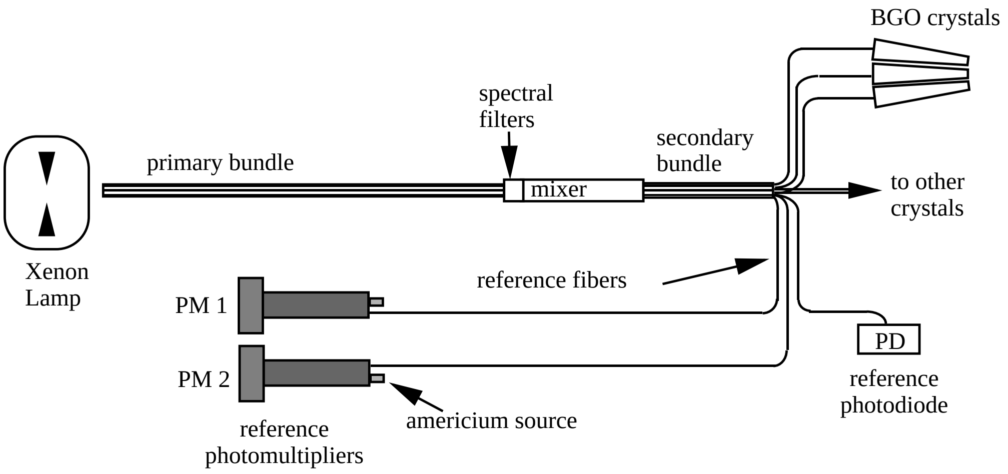

Figure 5.8: Schematic diagram of the Xenon monitoring system.

Figure 5.7 shows that the dead crystals were almost uniformly distributed and did not form dead regions in the BGO. To compensate for the energy loss caused by the BGO dead crystals, I developed a special algorithm, described in detail in Section C.2. This algorithm proved to be useful for both the RFQ calibration and the reconstruction of the electromagnetic showers.

5.3.3 Xenon Monitoring System

BGO light collection efficiency and electronics gain variations were monitored *in situ* with a Xenon flasher system [138, 139]. The system consisted of 32 Xenon lamps which generated light flashes with a spectrum tuned to match the spectrum of the BGO scintillation light. Light from each lamp was first transported to light mixers using bundles of optical fibers (*primary fiber bundles*) and then to the individual crystals using secondary fiber bundles (see Figure 5.8). The intensity of light from each mixer was measured with two reference photomultipliers, which were in turn monitored using γ rays from a radioactive ^{241}Am source. Both low and high gain electronics channels were studied using light pulses of different intensity, equivalent to about 1.1 GeV and 30 GeV.

Xenon calibration runs were performed on a daily basis and were very useful for

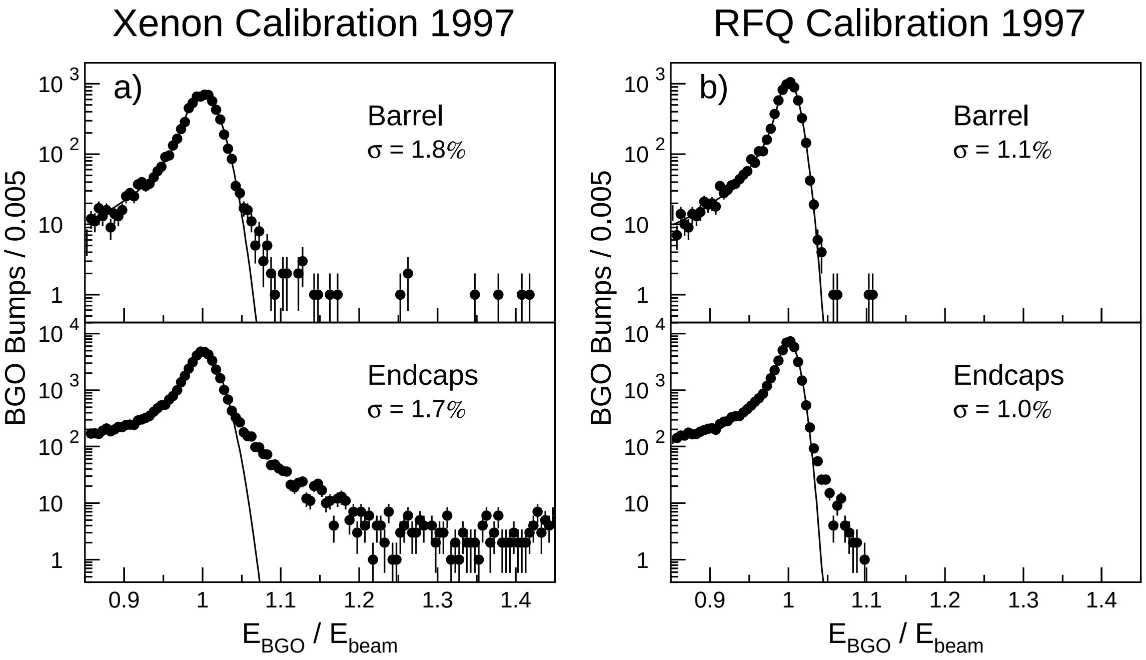

Figure 5.9: Energy distributions of Bhabha electrons selected in 1997 L3 data and reconstructed using a) Xenon and b) RFQ calibrations. The obtained BGO energy resolutions are shown on the plots.

monitoring the channel by channel BGO performance[12] and for studying the aging of the BGO [140]. Prior to 1997, the Xenon system was also used for the BGO calibration. The intercalibration of the BGO crystals was obtained using Xenon light flashes, while the absolute normalization was provided by Bhabha electrons. Energy resolutions of about 1.4% were achieved [134]. At the beginning of the LEP2 phase, the precision of the Xenon calibration started to deteriorate due to a significant decrease in the available Bhabha statistics.[13] In 1997 the BGO energy resolution obtained using Xenon calibration was about 1.8% with significant resolution tails,[14] as shown in Figure 5.9a. The test beam precalibration clearly showed that with an adequate calibration, the BGO calorimeter was capable of providing a sub-percent energy resolution. The goal of decreasing the calibration errors was achieved by the

---

[12] As described in the previous section.

[13] The cross section of the Bhabha scattering process was much lower at LEP2 than at LEP1.

[14] About 1.5% of Bhabha electrons in the endcaps and 0.7% in the barrel were reconstructed with $E_{shower}/E_{beam} > 1.1$.

RFQ calibration system, designed and built by the Caltech L3 group. Figure 5.9 shows a comparison between the Xenon calibration and the first successful RFQ calibration. The RFQ calibration system and method are described in the following sections.

5.4 RFQ Calibration Concept

In high-energy physics experiments, the task of calorimeter calibration is usually performed in two consecutive steps: 1) relative channel-to-channel calibration (*intercalibration*) and 2) adjustment of the absolute energy scale of the calorimeter (*absolute calibration*). At e^+e^- colliders, Bhabha scattering produces electrons with energy close to the beam energy and is widely used for the absolute calibration of electromagnetic calorimeters. In rare cases such as CLEO-II at CESR [141], the Bhabha production rate can be so high that no prior intercalibration is required. However, most often an intercalibration with a dedicated calibration system is necessary. For L3 at LEP2, the rate of useful Bhabha events in the BGO barrel was very low (2-3 Bhabha showers per crystal per year), and a rapid, reliable, and precise intercalibration of the BGO was of utmost importance. The Xenon monitoring system (see the previous section) was not able to intercalibrate the BGO calorimeter with the required 1% precision,[15] and a new intercalibration system was clearly needed.

Electromagnetic calorimeters are often intercalibrated with γ-rays from radioactive sources (e.g., at CUSB [142], Crystal Ball [143], and BaBar [144]). Unfortunately, the maximum photon energy easily available from a long-lived radioactive source is the 2.6 MeV line of ^{228}Th, which was much too close to the pedestal at L3 [145]. Cosmic rays can also be used as a calibration tool (e.g., at KLOE [146] and BELLE [147]). However, this technique was proven to be impractical for L3 since the required intercalibration precision of 1% could be achieved only after several months of dedicated running [148]. In order to solve the problem of the BGO intercalibration, the Caltech L3 group developed a novel calibration system based on a Radiofrequency Quadrupole

---

[15] The Xenon system was not able to directly test the scintillation mechanism of the BGO crystals. In addition, it was impossible to unfold the BGO aging from the aging of the optical fibers which were used to bring the light from Xenon flashlamps to the individual BGO crystals.

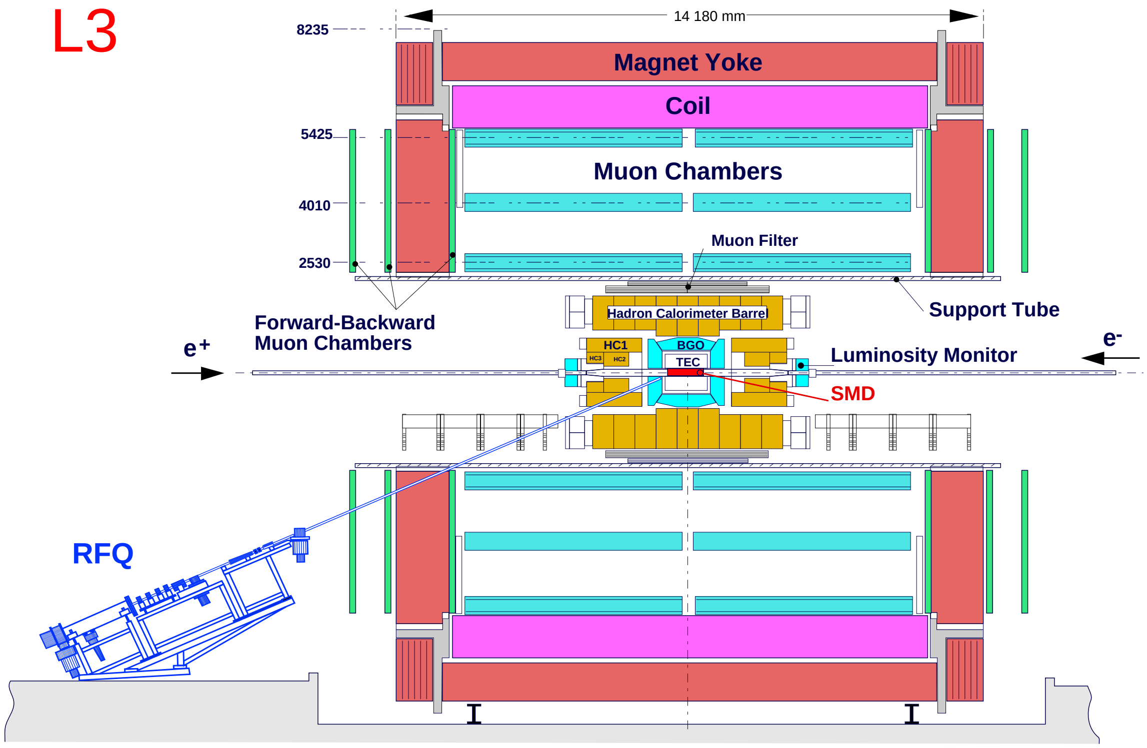

Figure 5.10: Side view of the RFQ system installed in L3.

(RFQ) accelerator. The principle behind the system was to bombard a lithium target, permanently installed inside the BGO calorimeter, with a pulsed H^- beam from the RFQ accelerator. After focusing and steering, the beam was neutralized to allow it to pass undisturbed through the L3 magnetic field. Radiative capture of protons

$$\mathrm{p} + {}^{7}_{3}\mathrm{Li} \rightarrow {}^{8*}_{4}\mathrm{Be} \rightarrow {}^{8}_{4}\mathrm{Be} + \gamma$$

produced a monochromatic flux of 17.6 MeV photons, which was used to simultaneously calibrate the entire BGO calorimeter on a crystal-by-crystal basis [149]. This particular nuclear reaction was chosen because it provides the highest photon energy attainable with non-cryogenic targets [145]. Figure 5.10 shows the installation of the RFQ system in the L3 detector.

5.5 The RFQ Calibration System

The RFQ calibration system was conceived and developed by the Caltech L3 group in 1984-1991 [150]. In 1992, it was installed in the L3 cavern and the inaugural *in situ* RFQ run was performed in 1993. After a major maintenance and upgrade of the system during the 1994-95 LEP shutdown, two successful high-statistics calibration runs were performed in 1995 giving the first RFQ calibration of the BGO [151].

The Crystal Ball experiment was the first to employ an accelerator (a Van de Graaf) as a calibration tool [143, 152]. However, the L3 RFQ calibration system was substantially more advanced as it was designed to provide a much higher beam intensity[16] and to be permanently installed in the detector. The last feature was essential given the size and complexity of L3 and required the use of an H^- ion beam coupled with a beam neutralizer. In addition, it imposed severe restrictions on the size of the system and on the designs of the RFQ beam pipe and target.

The RFQ calibration system consisted of the following components:

- A 30 keV RF-driven (2 MHz) volume H^- ion source with a maximum output current of 7.5 mA.
- A low-energy beam transport.
- A 1.85 MeV RFQ (425 MHz) accelerator, with a maximum output beam current of 35 mA.
- A high-energy beam transport comprising focusing and steering magnets.
- A beam neutralizer ($H^- \to H^0 + e^-$) consisting of a 1 m long N_2 gas cell, at a typical pressure of $5 \cdot 10^{-4}$ Torr, with a maximum neutralization efficiency of 55%.
- A 10 m long beam pipe, equipped with a star-cell ion pump (20 LPS) and a non-evaporable getter ribbon pump (3 LPS).

---

[16] The Crystal Ball experiment mainly used the nuclear reaction ${}^{19}_{9}\mathrm{F}(\mathrm{p},\alpha)\ {}^{16*}_{8}\mathrm{O}$ which has an order of magnitude larger cross section than the reaction ${}^{7}_{3}\mathrm{Li}(\mathrm{p},\gamma)\ {}^{8}_{4}\mathrm{Be}$ used in the L3 RFQ calibration [153]. Moreover, the BGO calorimeter had about 10 times more crystals than the NaI(Tl) main detector of the Crystal Ball.

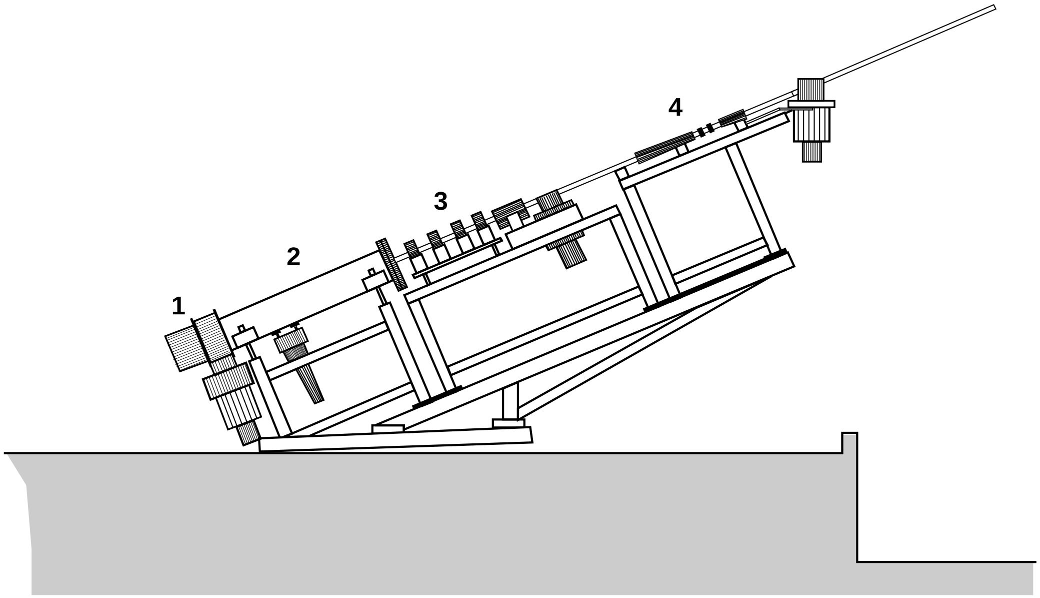

Figure 5.11: Schematic drawing of the RFQ system: 1) ion source; 2) RFQ accelerator; 3) steering and focusing magnets; 4) beam neutralizer.

- A water cooled LiH target, mechanically sealed with a thin Mo foil and mounted at the end of the beam pipe.
- Data acquisition and readout systems.

In order to protect the low energy ion beam from the fringe field of the L3 magnet, the RFQ accelerator, ion source, and neutralizer were enclosed inside a magnetic shield made of 15 mm thick mild-steel plates. A general view of the RFQ system is shown in Figure 5.11, and a detailed description of the RFQ system components can be found in Appendix B.

The RFQ calibration system proved to be reliable and robust. From 1995 to 2000, a total of nine RFQ calibration runs were performed, collecting a total of about 100 million triggers. Only one of the scheduled runs (Fall 1998) had to be canceled due to a malfunction in the ion source. The last calibration run performed in September 2000 showed no evidence of aging of the RFQ system hardware.

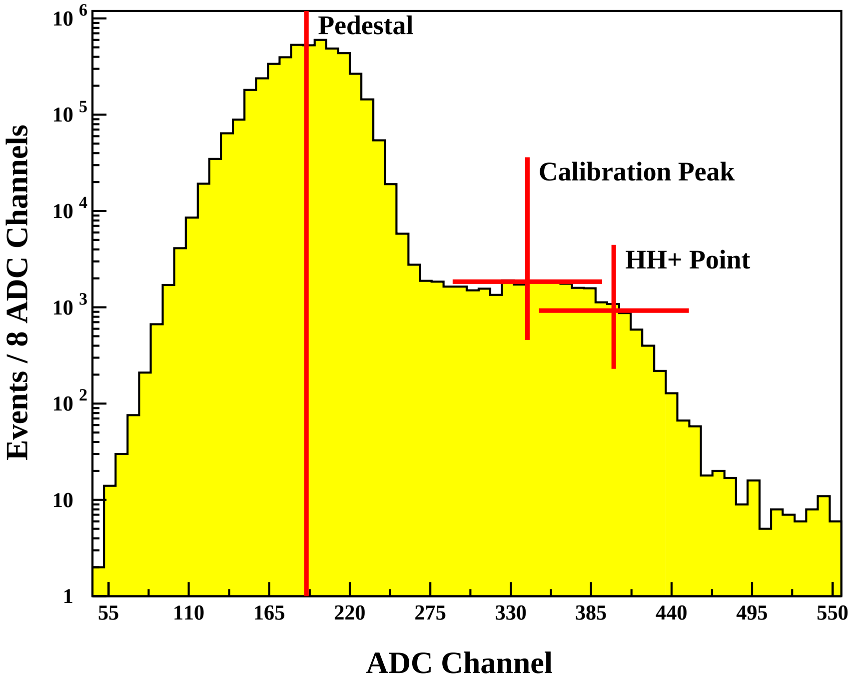

Figure 5.12: Typical energy spectrum of the photons produced by the RFQ system. Also shown is the definition of the HH^+ calibration point.

5.6 BGO Calibration

In this section I describe the methods that I developed and used to calibrate the BGO calorimeter using both the RFQ and LEP data. I also present the calibration results and briefly discuss how the RFQ experience can be used in calibrating the CMS electromagnetic calorimeter at the LHC.

5.6.1 Intercalibration with the RFQ System

The RFQ calibration runs were taken twice a year, before and after the annual LEP data taking run. Each RFQ run took three to five days to complete and, with an average DAQ rate of 80 Hz, produced about 10 million calibration triggers (beam pulses on target). As described in Section 5.4, the RFQ calibration was performed using 17.6 MeV photons produced by the radiative capture reaction ${}^7_3\mathrm{Li}(\mathrm{p},\gamma)\,{}^8_4\mathrm{Be}$. A typical photon energy spectrum recorded by a BGO crystal is shown in Figure 5.12.

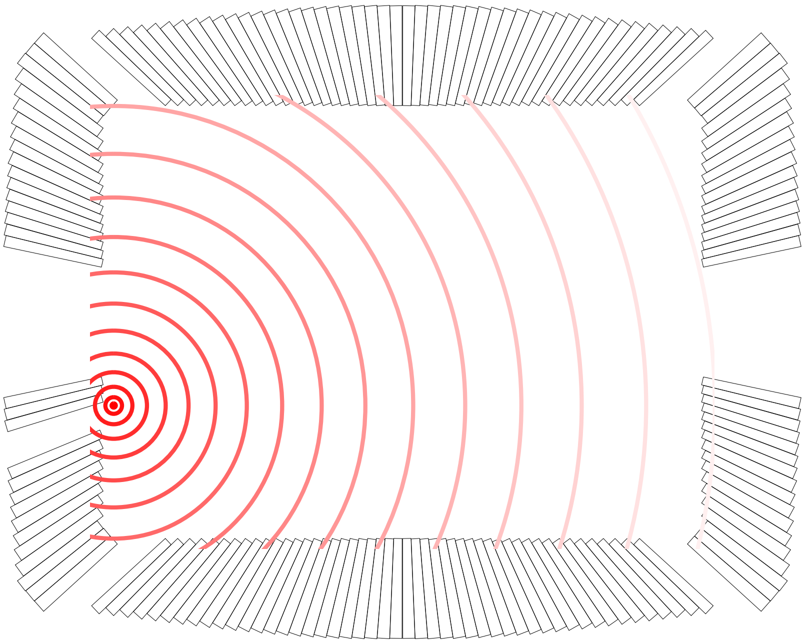

Figure 5.13: Side view of the BGO calorimeter with concentric circles representing the photon flux originating at the RFQ target.

The calibration constants were then derived as

$$\text{Calibration Constant(keV/ADC Count)} = \frac{E_{\mathrm{HH}^+}}{\mathrm{HH}^+ - \mathrm{Pedestal}}\,, \tag{5.6}$$

where E_{HH^+} was assumed to be equal to 17.6 MeV and the "HH^+" edge was the specific feature used for calibration and defined as the point half-way below and to the right of the calibration signal peak (see Figure 5.12). Figure 5.13 shows that the RFQ target was significantly off-center with respect to the BGO calorimeter. As a result, the incident photon angle and the amount of material in front varied from crystal to crystal. Previous studies[17] had shown that while the HH^+ point was the least sensitive to these systematic effects, the induced variations in the actual values of E_{HH^+} could be as high as 2-3% [150, 155]. These geometrical effects were corrected for by the absolute calibration with Bhabha events, as described in the next section.

The position of the HH^+ point was found using a simple *moving window* algorithm.

---

[17] Including Monte Carlo studies [150, 154] and beam tests with a Van de Graaf at Caltech [150] and with an RFQ at AccSys Technology [150, 155].

The procedure started with finding the maximum of the signal peak by defining three adjacent windows and assuming that the spectrum was parabolic in the windowed region. The windows were slid along until the estimated maximum was found within the windowed region. The maximum was then computed as a weighted average of the values obtained by varying the window sizes from 16 to 48 ADC counts. After the maximum was found, the HH$^+$point was obtained with a similar method which used two adjacent windows and assumed that the spectrum was linear in the windowed region. Another method of finding the HH$^+$ point by using a cubic spline fit had also been tested and gave similar results [150].

Calibration Results

The rate of calibration photons per crystal was characterized by the *photon occupancy*, defined as the fraction of triggers with energy deposition in one crystal larger than 14 MeV. Because of the off-center location of the RFQ target, the occupancy differed from crystal to crystal and was significantly higher for the RB24 half of the BGO calorimeter (the side closer to the RFQ target). Figure 5.14 shows the photon occupancy for the calibration run performed in September 2000. The typical crystal occupancy was about 0.008% for the near side (RB24) and about 0.004% for the far side (RB26).

As discussed in Section B.5, a veto scheme was implemented to reject photons not contained in a single crystal. Because of this, the highest calibration efficiency was achieved when the average occupancy was about 1-2% [149]. The intensity of the calibration photon flux was below this optimum level mainly because the ion source was not capable of delivering a sufficiently high H$^-$ current (see Section B.1.1).

The BGO temperature was monitored during the RFQ runs and the calibration constants derived from Equation 5.6 were corrected to the reference temperature of 18°C using Equation 5.5. Calibration constants obtained from the September 2000 RFQ run are shown in Figure 5.15, and the typical calibration constant value is about 90 keV/ADC Count. Comparing Figures 5.14 and 5.15, one can see that contrary to the distribution of the crystal occupancy, the spatial distribution of the calibration

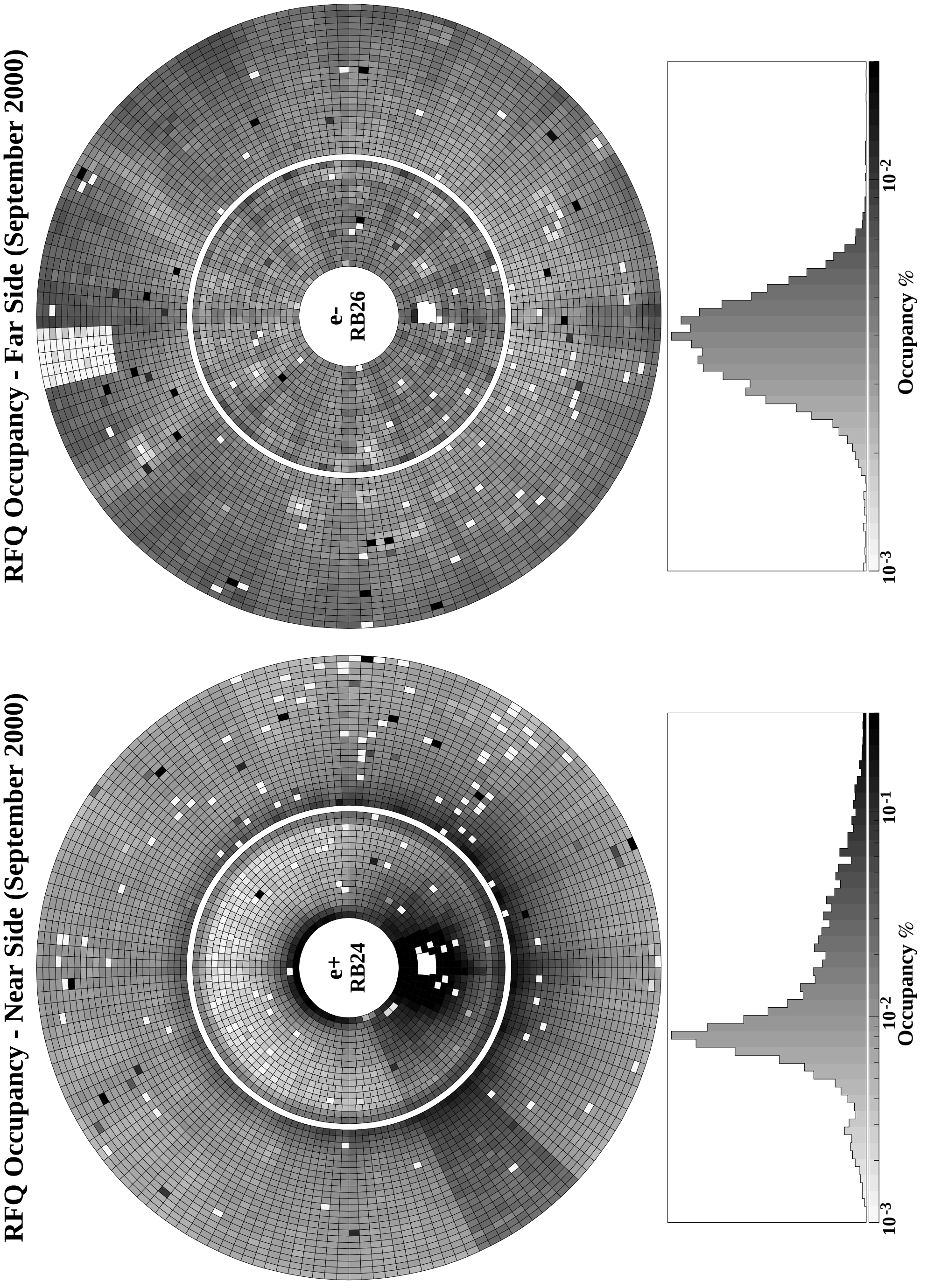

Figure 5.14: Crystal occupancy for the September 2000 RFQ run. The inner and outer rings represent the endcaps and half-barrels, respectively. The holes in the endcaps are for the RFQ beam pipe.

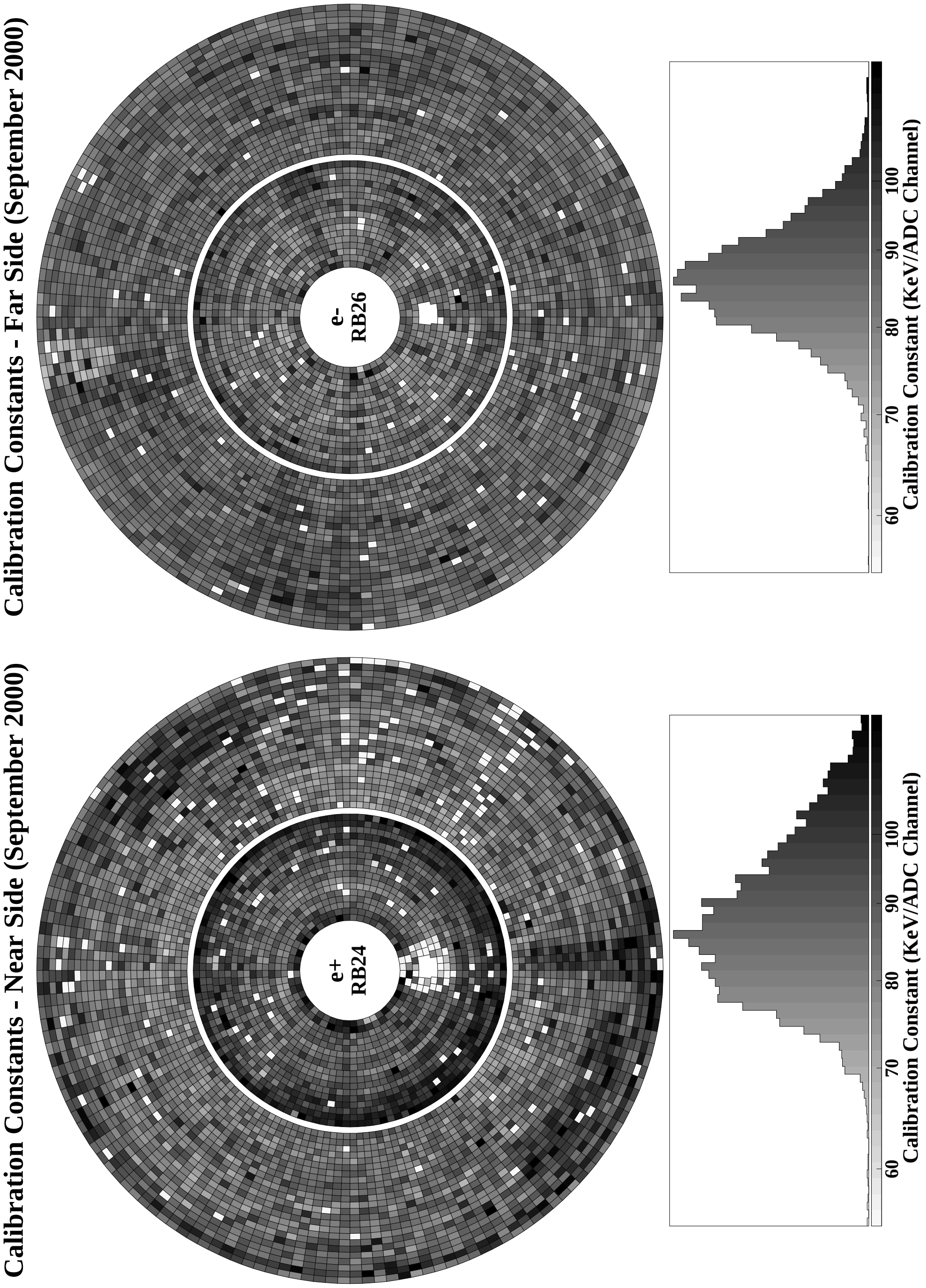

Figure 5.15: Calibration constants from the September 2000 RFQ run. The inner and outer rings represent the endcaps and half-barrels, respectively. The holes in the endcaps are for the RFQ beam pipe.

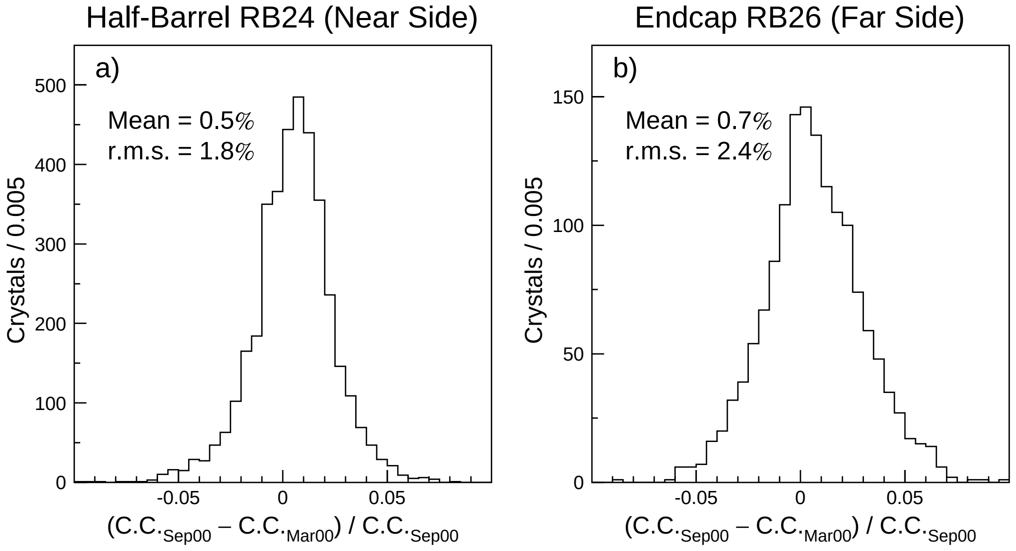

Figure 5.16: Relative difference between the two sets of calibration constants derived from the March and September 2000 RFQ runs. Shown are the distributions for the near side barrel and far side endcap.

constants was relatively uniform across the BGO and unaffected by various systematic effects such as the off-center location of the RFQ target and electronic noise in the readout segments of the BGO calorimeter.

The statistical precision of the intercalibration can be estimated by plotting the relative difference between constants obtained from two independent runs, as shown in Figure 5.16 for the two runs taken in the year 2000. The RMS width of this distribution shows that the statistical uncertainty on the RFQ calibration constants[18] was about 1% for all four parts of the calorimeter.[19] The non-zero shift in the average constant value is consistent with the aging of the BGO response (see Section C.3).

However, the total error of the RFQ calibration was dominated by the systematic uncertainties, as can be seen from Figure 5.17, which shows the energy distribution of Bhabha electrons reconstructed using a set of the RFQ calibration constants. The overall precision of the intercalibration was determined to be about 2% in the barrel

---

[18] Calibration constants from the semiannual RFQ runs were usually averaged, and the obtained set of constants was used as a starting point for the annual absolute calibration of the BGO.

[19] It should be also noted that this estimate is consistent with the values obtained from an early test at AccSys Technology [150] and from the first *in situ* RFQ calibration runs at L3 [151].

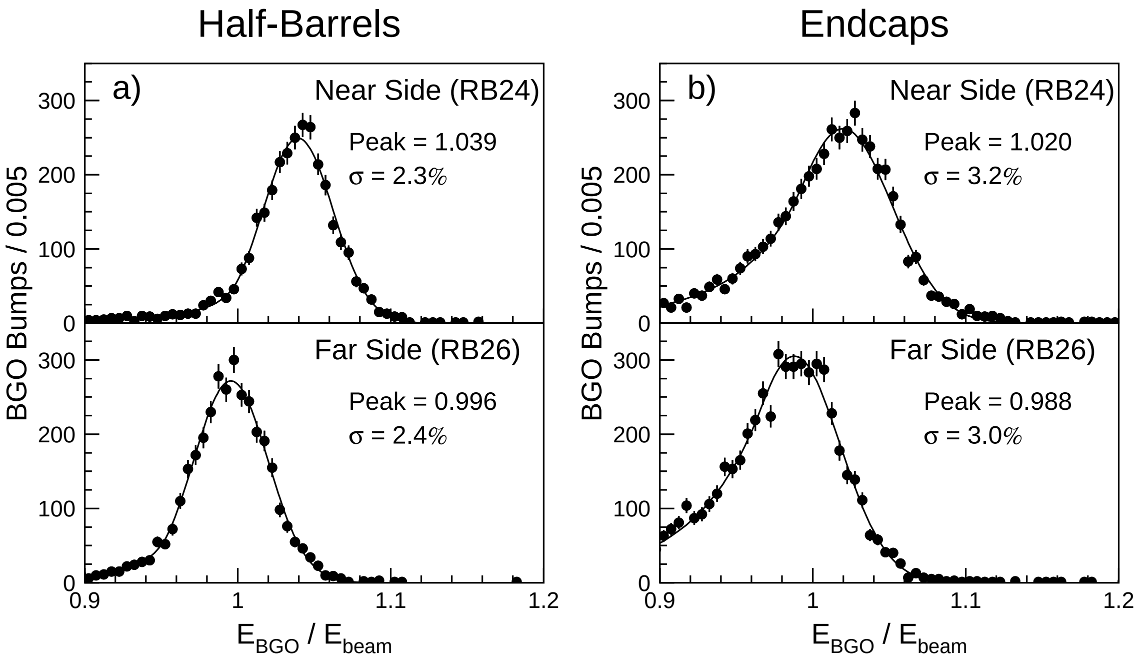

Figure 5.17: Energy spectra of Bhabha electrons reconstructed using a set of the RFQ intercalibration constants, a) in the barrel and b) in the endcaps. The peak positions and resolutions are indicated on the plots.

and 3% in the endcaps. The quality of the intercalibration was worse in the endcaps due to the more complicated geometrical effects. The RFQ target was located very close to the surface of the near side endcap (RB24), producing significant variations in the photon incident angle. For the far side endcap (RB26), the propagation of the calibration photon flux was perturbed by the TEC end-flange, a 5 cm thick aluminum plate.

In addition to the geometrical effects, the calibration precision was affected by the nonlinearity of the BGO response, as we had to extrapolate from the 17 MeV energy scale of the calibration up to the $\mathcal{O}(10\text{ GeV})$ scale of physics at LEP. Figure 5.17 shows that the geometrical effects also induced a noticeable shift (1-2% depending on the subdetector) in the absolute scale of the RFQ calibration. However, the above systematic effects were time-independent and thus could be easily corrected for using Bhabha electrons, as described in the next section.

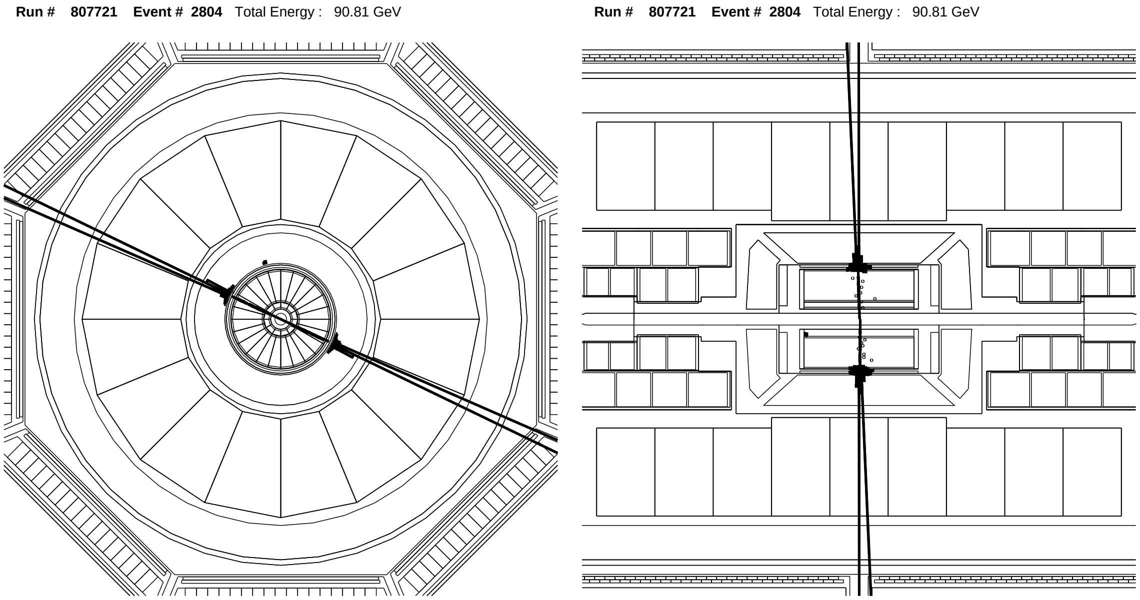

Figure 5.18: A typical back-to-back Bhabha scattering event recorded by the L3 detector at $\sqrt{s} = 91.2$ GeV and displayed in the $x - y$ and $x - z$ planes. Tracks reconstructed in the TEC are shown as back-to-back lines originating near the primary vertex. Energy deposits in the BGO crystals are shown as towers whose height is proportional to the crystal energy.

5.6.2 Absolute Calibration with Bhabha Events

Selection of Bhabha Events

The Bhabha scattering process, $\mathrm{e^+e^-} \rightarrow \mathrm{e^+e^-}(\gamma)$, is widely used in calibration of electromagnetic calorimeters because it produces events with back-to-back electrons whose energy is kinematically constrained to be close to the beam energy, which is usually known to a very high precision ($0.01 - 0.02\%$ at LEP). A typical back-to-back Bhabha event recorded by the L3 detector in April 2000 is shown in Figure 5.18. Therefore, the first step of the absolute calibration was to select a sample of such Bhabha events. The selection criteria that I used are listed below:

Fiducial volume

$42^\circ < \theta_{1,2} < 138^\circ$ (barrel) and $10^\circ < \theta_{1,2}(180^\circ - \theta_{1,2}) < 37^\circ$ (endcaps), where θ_1 and θ_2 denote the polar angles of the two most energetic bumps. This cut ensured that the most energetic bumps were both in the BGO barrel or both in the endcaps.

Shower energies $E_1 > 0.8 \cdot E_{beam}$ and $E_2 > 0.5 \cdot E_{beam}$,
where E_1 and E_2 were the energies of the two most energetic bumps and E_{beam} was the beam energy. This cut rejected most of the $e^+e^- \rightarrow \tau^+\tau^-$ background.

Acollinearity $\zeta < 5°$,
where ζ was the acollinearity angle between the two most energetic bumps.[20] This was the most important cut of the selection as it rejected most of the radiative Bhabha events, $e^+e^- \rightarrow e^+e^-\gamma$, and ensured that the selected events contained only back-to-back showers. Without this cut, as much as 20% of the Bhabha events were expected to include at least one electron with energy below $0.9 \cdot E_{beam}$ since a significant fraction of energy could be carried away by initial and final state photon radiation.

Transverse shower profile $S_9^c/S_{25}^c > 0.94$.
This requirement was widely used in L3 to reject showers originating from hadrons and cosmic rays. It ensured that both BGO bumps had the shower profile consistent with the one expected for an electron or a photon. More than 99% of Bhabha showers were expected to pass this cut.

Longitudinal shower profile $E_{\mathrm{HCAL}}/E_{\mathrm{BGO}} < 0.08$,
where E_{BGO} was the bump energy as measured by the BGO and E_{HCAL} was defined as a sum of energies of the HCAL clusters in a 10° cone around the bump direction. This requirement rejected showers with significant leakage into the hadron calorimeter. More than 98% of Bhabha showers were expected to pass this cut. The performance of these shower-shape cuts will be discussed in more detail in Section 6.3.1 of Chapter 6.

No other significant activity in the detector $E_{vis} - E_{\mathrm{BGO}} < 5$ GeV and $E_3 < 0.3$ GeV,
where $E_{vis} - E_{\mathrm{BGO}}$ gave the energy not assigned to the identified BGO bumps and E_3 was the energy of the third most energetic shower in the BGO, if any.

This selection is similar to the BGO-based Bhabha selection which was widely used at LEP1 [151]. Since no information from the tracking system of L3 was used,

---

[20] About 20% of the showers were either near the calorimeter edges or had a dead channel in the 3×3 matrix around the bump crystal. For events with at least one such shower, the acollinearity cut was relaxed to 8°.

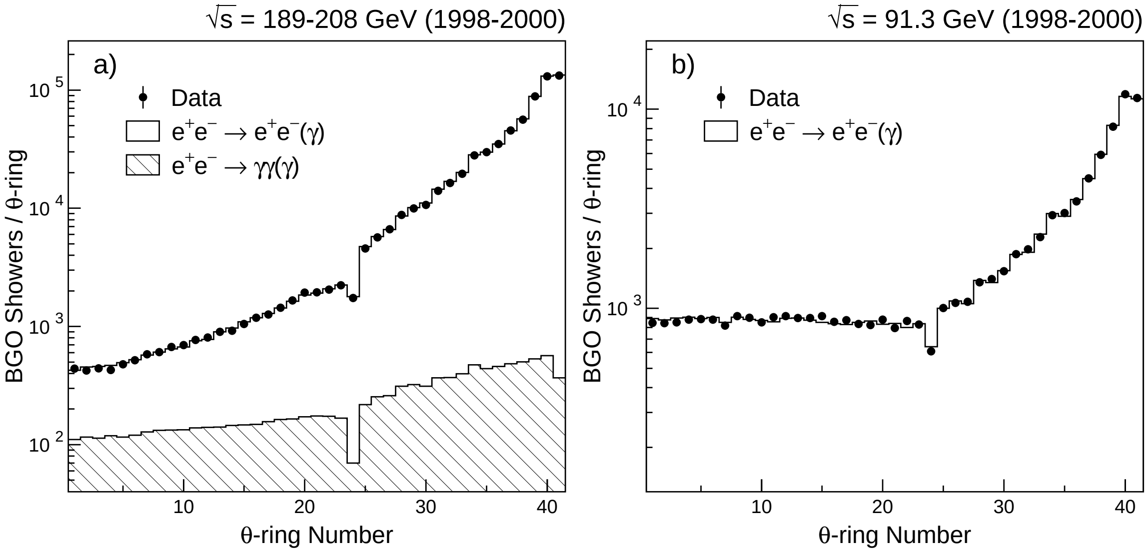

Figure 5.19: θ-ring distribution of the back-to-back showers used in the absolute calibration of the BGO. Shown are the distributions for the samples selected in 1998-2000 at a) $\sqrt{s} = 189 - 208$ GeV and b) $\sqrt{s} = 91.3$ GeV. Here the θ-ring number refers to the location of the central crystal of the electromagnetic shower.

events from the collinear photon (di-photon) production process, $e^+e^-\rightarrow\gamma\gamma(\gamma)$, were also accepted. At Born level, this is a well-understood QED process with a cross section significantly smaller than that of the Bhabha scattering.

Figure 5.19a shows the θ-ring[21] distribution for events selected in 625 pb^{-1} of data collected by L3 during 1998-2000 at $\sqrt{s} = 189-208$ GeV. Also shown are the expected distributions for the Bhabha scattering and collinear photon production, which are obtained using the `BHWIDE` [156] and `GGG` [157] Monte Carlo generators, respectively. Good agreement between data and Monte Carlo predictions was observed. The number of selected events increased sharply with the θ-ring number and was much higher in the endcap region ($N_{\theta-\mathrm{ring}} > 24$). This was because at LEP2 energies the Bhabha scattering proceeded predominantly through the t-channel electron exchange so that its differential cross section rose steeply at low polar angles.

However, in the BGO barrel the production cross section at high center-of-mass

---

[21] As described in Section 4.2.3, each BGO half-barrel and endcap consisted of 24 and 17 individual θ-rings, respectively (see Figures 4.9 and 4.11).

energies was rather small: at $\sqrt{s} = 200$ GeV $\sigma_{\mathrm{e^+e^-}} = 22$ pb and $\sigma_{\gamma\gamma} = 4$ pb [135, 158]. To increase the calibration statistics, I also used data from *Z-peak* LEP runs.

During each year of the LEP2 program, 15-20 days were dedicated to LEP runs at the Z peak, $\sqrt{s} = 91.3$ GeV, and the collected samples of two-fermion events were used to calibrate the LEP detectors.[22] At the Z peak, the Bhabha scattering reaction was dominated by the s-channel Z exchange, and its production cross section in the barrel region was significantly higher: $\sigma_{\mathrm{e^+e^-}(\gamma)} \simeq 1$ nb [151]. During 1998-2000, the L3 detector recorded a total of 11.1 pb^{-1} of data at $\sqrt{s} = 91.3$ GeV. The corresponding θ-ring distribution of the selected Bhabha showers is shown in Figure 5.19b.

Combining the two selected samples gave a total of about 50,000 and 850,000 calibration showers for the BGO barrel and endcaps, respectively. In order to improve the calibration precision in the barrel, I also selected a sample of about 20,000 Bhabha events using 30.1 pb^{-1} of data collected in 1995 at or near the Z resonance. It should be noted that the back-to-back Bhabha and di-photon events could be used not only for the absolute calibration of the BGO, but also for the studies of the BGO aging and non-linearity, as described in Appendix C.

Iterative Calibration Algorithm

After the event samples had been selected, the absolute calibration scale could be set using an iterative calibration algorithm which exploited the fact that the showers in the selected back-to-back e$^+$e$^-$ and $\gamma\gamma$ events were kinematically constrained to have an energy close to the beam energy. The calibration constant for a given crystal was obtained as follows [159]:

$$\mathcal{C}_N(n_\theta, n_\phi, n_z) = \mathcal{C}_{N-1}(n_\theta, n_\phi, n_z) \cdot \frac{1}{\sum_{i=1}^{n_{bumps}} w_i} \sum_{i=1}^{n_{bumps}} \frac{E_{beam}}{E_i} w_i \,, \tag{5.7}$$

where

1. N was the iteration step number.

---

[22] The $\mu^+\mu^-$ events were used to calibrate the muon chambers and the charged particle trackers, the $\mathrm{q\bar{q}}$ events provided the jet energy scale, and the Bhabha scattering events were used to calibrate the trackers and electromagnetic calorimeters.

2. $\mathcal{C}(n_\theta, n_\phi, n_z)$ was the calibration constant.
3. n_θ, n_ϕ, and n_z were the coordinates of the crystal — n_θ was the θ-ring number, n_ϕ gave the ϕ-coordinate, and $n_z = 1, 2$ corresponded to the two halves of the BGO calorimeter (RB24 and RB26).
4. n_{bumps} was the number of the selected BGO bumps containing this crystal in the 3×3 crystal matrix centered on the crystal with the maximum energy deposition.
5. E_{beam} was the beam energy.
6. E_i was the energy (corrected sum-of-nine) of the ith bump computed using the raw ADC signals and the calibration constants from the previous iteration step, $\{\mathcal{C}_{N-1}\}$, according to Equations 5.1 and 5.2.
7. w_i was the weight assigned to the ith event for the crystal, which I chose to be equal to the ratio of the energy deposited in the crystal to the total energy deposited in the 3×3 crystal matrix, where these energy quantities were also computed using the calibration constants $\{\mathcal{C}_{N-1}\}$ and the raw ADC signals.

The initial set of constants, $\{\mathcal{C}_0^{\mathrm{RFQ}}\}$, was provided by the RFQ intercalibration.[23] Since the available Bhabha statistics was limited and the precision of the RFQ intercalibration was quite high, five or six iteration steps were usually sufficient to reach the maximum calibration precision, and no significant improvement could be obtained by increasing the number of iterations.

To further reject radiative Bhabha events, only bumps with an energy above $0.95 \cdot E_{beam}$ were used in the calibration. In addition, to minimize systematic effects from the BGO non-linearity and electronic noise, a BGO bump was not used ($w_i = 0$) if the energy deposited in the crystal in question was below 2 GeV.

For the endcaps where the Bhabha statistics was relatively high, only events selected in L3 data from the two most recent years were used in the calibration. For the

---

[23] The RFQ constants for the four BGO subdetectors were first multiplied by four different constant factors to correct for the overall shift induced by the geometrical effects, i.e., to bring the overall normalization of the Bhabha peaks in Figure 5.17 to one.

barrel, the entire available sample of the back-to-back events from LEP2 (1998-2000) had to be used. Moreover, Bhabha events from the 1995 data sample were used to correct for the geometrical systematic effects in the following way. First, a set of the calibration constants, $\{\mathcal{C}^{95}\}$, was obtained using Equation 5.7, where the starting set of constants, $\{\mathcal{C}_0^{\mathrm{RFQ95}}\}$, was provided by the two RFQ calibration runs taken in 1995.[24] A set of correction factors was then calculated as

$$\{\mathcal{F}_{\mathrm{corr}}\} = \frac{\{\mathcal{C}^{95}\}}{\{\mathcal{C}_0^{\mathrm{RFQ95}}\}}\,. \tag{5.8}$$

The correction factors were applied to the barrel intercalibration constants before running the iterative procedure on the selected LEP2 Bhabha sample. This procedure was found to improve the calibration precision because the majority of the systematic errors on the RFQ intercalibration constants were time-independent, as discussed in Section 5.6.1.

The absolute calibration was performed with data collected during the last three year of the LEP2 program (1998-2000) at center-of-mass energies ranging from 91 GeV to 208 GeV. Therefore, additional correction factors had to be applied to take into account the aging and energy non-linearity of the BGO response. These correction factors were determined by complementary studies of the BGO performance, described in Appendix C, Sections C.3 and C.4.

About 20% of the BGO showers were either near the calorimeter edges or had a dead channel in the 3 × 3 matrix. Such showers were also included in the selected Bhabha samples in order to calibrate the edge crystals and crystals adjacent to the dead channels. The resulting shower energy mismeasurement had to be estimated and corrected for on an event-by-event basis. A detailed description of this procedure is given in Appendix C, Section C.4.

In the L3 BGO, a multi-GeV electromagnetic shower would typically spread over the 3 × 3 crystal matrix and was reconstructed using energy depositions in all nine

---

[24] It is interesting to note that the derived set of the calibration constants, $\{\mathcal{C}^{95}\}$, provided a better energy resolution than the "official" BGO calibration used in the reconstruction of the 1995 L3 data (1.3% *vs.* 1.8%).

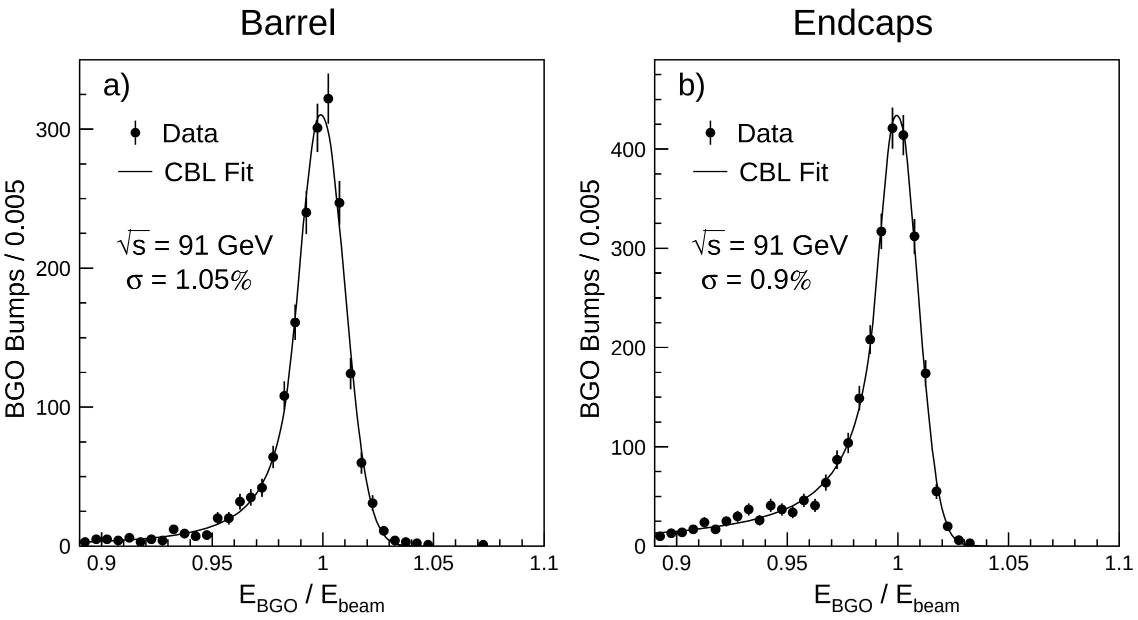

Figure 5.20: Energy spectrum of the unbiased Bhabha sample selected in the L3 Z-peak data collected in 2000 at $\sqrt{s}$ = 91.3 GeV a) for the BGO barrel and b) for the BGO endcaps. The peak positions and resolutions are indicated on the plots.

crystals of the matrix. The iterative calibration algorithm that I developed took this effect into account, thus providing a clear advantage over the algorithms used in the 1987-88 beam tests and at LEP1, which calibrated only the central crystal of the shower [131, 139]. At the same time, this algorithm was robust — all 11,000 crystals of the calorimeter could be calibrated in less than an hour (using a 1 GHz Linux box). In addition, it provided a straightforward way to correct for the non-linearity and aging of the calorimeter response.

5.6.3 Calibration Results

BGO Energy Resolution

An unbiased measurement of the BGO energy resolution was performed with Bhabha events not included in the sample used for the absolute calibration.[25] Figure 5.20 shows that for 45 GeV electrons, the achieved energy resolution was 1.05% in the

---

[25] Each year, a third of the Bhabha events from the Z-peak calibration runs were used to test the calibration precision.

Source of uncertainty	Magnitude of uncertainty [%]	
	Barrel	Endcaps
“Intrinsic” resolution	0.80 ± 0.03	0.71 ± 0.03
Temperature fit	0.45 ± 0.15	0.45 ± 0.15
RFQ calibration	0.52 ± 0.16	0.38 ± 0.21
BGO energy resolution	1.05 ± 0.04	0.92 ± 0.04

Table 5.2: Factors contributing to the relative BGO energy resolution (in %) for 45.6 GeV electrons.

barrel and 0.9% in endcaps. The peak position and resolution were obtained by fitting the spectrum to a lineshape function which was first used by the Crystal Ball experiment and is referred to as “CBL Fit” on the plot. This was done to take into account the peak distortion and the low-energy tail induced by the initial state radiation (for more details see Section C.1).

Other factors contributing the energy resolution were the intrinsic resolution of the calorimeter and the temperature measurement errors, as discussed in Sections 5.2 and 5.3.1, respectively. The calibration error could then be evaluated by subtracting these factors in quadrature, and was found to be 0.5% for the BGO barrel and 0.4% for the BGO endcaps, i.e., about three times smaller compared to that at LEP1 and at the beginning of LEP2. Table 5.2 summarizes the sources of uncertainty contributing to the BGO energy resolution for 45 GeV electrons. One can see that contrary to the case of LEP1, at LEP2 the calibration error was no longer the dominant source of uncertainty on the energy measurement for multi-GeV electrons and photons.

In addition to the improvement in the BGO resolution, the *RFQ+Bhabha* calibration also eliminated the problem of the high-energy resolution tails, as can be seen by comparing Figures 5.9a and 5.20. This was crucial for many L3 analyses at LEP2, including the one presented in this thesis.

For the BGO barrel, the energy resolution as a function of shower energy was derived by adjusting the constant term in the expression for the BGO intrinsic resolution given by Equation 5.4. This procedure was justified because both the calibration and temperature fit errors were energy-independent and, thus, contributed only to the constant term. The obtained resolution function was

$$\frac{\sigma_E}{E}(\text{barrel}) = \frac{3.1 \pm 0.3\ \%}{\sqrt{E}} \oplus 0.9 \pm 0.1\ \%\ (E \text{ in GeV})\,, \tag{5.9}$$

where the errors were estimated using the measured widths of the Bhabha peak (see Table 5.2) and the π^0 and η mass peaks, which were reconstructed as discussed below. In a similar fashion, the energy resolution for the endcaps was found to be:

$$\frac{\sigma_E}{E}(\text{endcaps}) = \frac{3.3 \pm 0.3\ \%}{\sqrt{E}} \oplus 0.8 \pm 0.1\ \%\ (E \text{ in GeV})\,. \tag{5.10}$$

The angular resolution of the BGO was also studied and the obtained resolution functions are summarized in Appendix C, Section C.5.

The validity of these equations for lower energies was verified using a sample of π^0 mesons selected in hadronic events ($e^+e^- \to q\bar{q}$) from the 1999 Z-peak calibration data. The π^0 mesons decay predominantly into two photons, $\pi^0 \to \gamma\gamma$. Therefore the event selection required two photons with energies above 1 GeV and 0.3 GeV for the most and least energetic photons, respectively [160]. The $\gamma\gamma$ invariant mass distribution for such two photon combinations is shown in Figure 5.21a. The obtained π^0 mass resolution of $\sigma_{DATA}(\pi^0) = 8.0 \pm 0.2$ MeV was well reproduced by the Monte Carlo simulation which gave $\sigma_{MC}(\pi^0) = 7.8 \pm 0.1$ MeV [161].

In the same way, the η resonance could also be measured in its two-photon decay mode. Figure 5.21b shows the η mass distribution reconstructed using the hadronic Z-decays at LEP1 [162]. Here both photons were required to have an energy above 0.5 GeV, and the typical photon momentum was harder than the momentum of the photons from π^0 decays. A Gaussian fit to the η peak gave a width of $\sigma_{DATA}(\eta) = 16.1 \pm 0.6$ MeV, in good agreement with the Monte Carlo prediction of $\sigma_{MC}(\eta) = 16.3 \pm 0.2$ MeV.

Similar studies performed using L3 data collected during 1994-2000 also showed a good agreement between the data and Monte Carlo simulations [161, 163]. It can

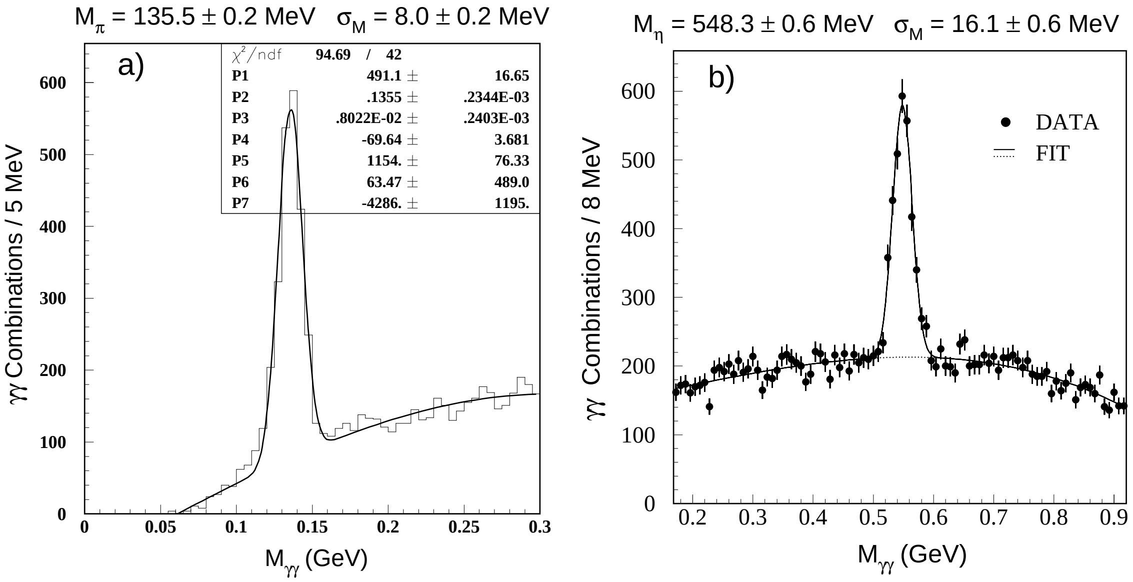

Figure 5.21: The $\gamma\gamma$ invariant mass distributions showing a) the π^0 mass peak measured using hadronic events from the 1999 Z-peak calibration data [160], and b) the η mass peak measured using the LEP1 data [162]. The peak positions and widths are indicated on the plots.

be therefore concluded that Equations 5.9 and 5.10 adequately describe the BGO energy resolution down to $E_\gamma \simeq 1$ GeV, i.e., for the entire energy range studied in this thesis.[26]

The absolute calibration of the BGO was performed mainly with electrons, while the subject of this thesis consists of studying single- and multi-photon events. As discussed in Section 4.2.3, electromagnetic showers produced by multi-GeV photons and electrons developed in a similar fashion, and the BGO response was expected to be essentially the same for both types of showers. This was also confirmed by the Monte Carlo simulations of the detector response.

As a cross check, I compared the BGO resolution for 100 GeV photons and electrons using back-to-back Bhabha and di-photon events selected in the high-energy data collected in 2000 at $\sqrt{s} = 205 - 208$ GeV. The main event selection criteria that I used are listed in the previous section. An additional cut requiring two charged tracks matching with the BGO bumps was applied for the $e^+e^- \to e^+e^-$ candidates,

---

[26] A more accurate resolution function for sub-GeV showers can be found in Reference [110].

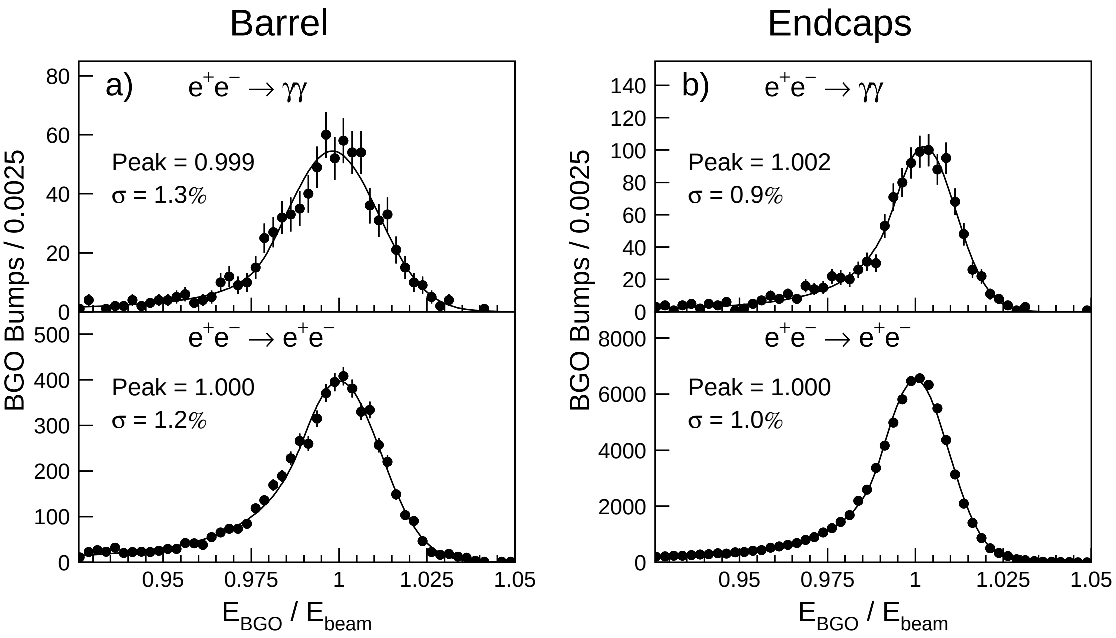

Figure 5.22: Energy spectra of the back-to-back Bhabha and di-photon events selected in the 2000 data collected at $\sqrt{s} = 205 - 208$ GeV a) for the BGO barrel and b) for the BGO endcaps. The peak positions and resolutions are indicated on the plots. For the di-photon spectra, the statistical errors on the peak positions and widths are about 0.001 and 0.1%, respectively.

while the $e^+e^- \to \gamma\gamma$ events were selected by requiring no significant activity in the TEC. To avoid biases, I used calibration constants from the year 1999.[27]

As shown in Figure 5.22, the peak positions and widths for the electron and photon energy spectra were statistically compatible, indicating that the calibration procedure did not introduce any significant systematic bias in the BGO response to multi-GeV photons. It should be noted that since the shower energies were reconstructed using the 1999 calibration constants, the measured values of the BGO resolution were slightly worse than predicted by Equations 5.9 and 5.10.

Calibration of the CMS Electromagnetic Calorimeter

The electromagnetic calorimeter of the CMS detector at the LHC will consist of 77,200 lead tungstate crystals and has a design goal of measuring electrons and photons

---

[27] The 1999 calibration constants were multiplied by constant factors to take into account the BGO aging.

with an energy resolution of better than 1% over a large energy range. Such a high resolution will be needed to maximize the sensitivity to the Higgs boson[28] in the two-photon decay channel, H → $\gamma\gamma$ [164].

Achieving a precise *in situ* calibration is the key to maintaining the calorimeter resolution at the design level. The experience gained in calibrating the L3 BGO calorimeter at LEP has already proved to be very useful for the development of the calibration strategy at CMS. The example of L3 shows that achieving a ~ 0.5% calibration precision in a challenging physics environment is feasible. However, it also shows that the calorimeter calibration is not an easy task and that without an adequate preparation, it may take several years to develop necessary calibration tools and methods. To avoid repeating the mistakes of L3, four CMS teams, including the Caltech team, are conducting considerable research in this area.

The calibration of the CMS ECAL will also be performed in two stages. The intercalibration will be carried out using a laser-based monitoring system, built by the Caltech group [165]. While the absolute calibration is expected to be achieved using physics events from the $W \to e\nu$, $Z \to e^+e^-$, and $\eta(\pi^0) \to \gamma\gamma$ processes [166, 167].

In the CMS ECAL, a multi-GeV electromagnetic shower will not be contained in a single crystal and a 5×5 crystal array will be used to reconstruct its energy and position in a manner similar to the one used for the BGO bumps (see Section 5.1). Thus, a special calibration algorithm is needed to take this effect into account. To address this problem, the CMS groups working on the absolute calibration of the ECAL are now using the L3 iterative calibration algorithm that I developed. Not only is this algorithm simple and robust, but studies have also shown that it performs as well as a more complex calibration algorithm based on the Householder method for solving linear equations [166].

---

[28] The Higgs discovery is the main goal of the LHC program and H → $\gamma\gamma$ is one of the most promising decay channels.

Conclusion

During 1997-2000, the L3 BGO calorimeter was successfully calibrated with the RFQ calibration system and Bhabha events. A calibration precision of about 0.5% was achieved and the BGO design goal of 1% energy resolution was reached for the first time since the 1987-88 beam tests. The RFQ calibration was used in the L3 data reconstruction and was shown to significantly improve the quality of several physics analyses, including the one presented in this thesis.

The experience gained in calibrating the L3 BGO at LEP is now successfully used for the calibration of the CMS lead tungstate calorimeter. Complementary studies of the BGO performance, including the studies of the BGO non-linearity and aging are presented in Appendix C.